PERGAMON

International Journal of Plasticity 17 (2001) 971–990

INTERNATIONAL JOURNAL OF Plasticity

www.elsevier.com/locate/ijplas

A robust integration-algorithm for a finite-strain shape-memory-alloy superelastic model

Ferdinando Auricchio *

Dipartimento di Meccanica Strutturale, Università di Pavia, Via Ferrata 1, 27100 Pavia, Italy

Received in final revised form 3 June 2000

Abstract

An interesting feature of *shape-memory alloys* (SMA) is the *superelastic* effect, that is, the ability to undergo large deformations in loading–unloading cycles without showing permanent deformations. Due to this macroscopic behavior, not present in traditional materials, shape-memory alloys are exploited in innovative applications, often requiring the use of design tools. The present work proposes an efficient and robust solution algorithm to be used during the design of SMA-based devices through the use of classical computational tools such as the finite element method. To reach this goal, we review a constitutive model able to reproduce the superelastic behavior at finite strains. We then discuss a solution algorithm for the corresponding time-discrete model. Cast within the return-map family, the adopted approach pays particular attention to the overall algorithmic robustness and to the possibility of an efficient implementation. To properly test the proposed approach, we start solving a series of severe one-dimensional tests. We then also simulate a complex three-dimensional problem, relative to an orthodontic archwire. © 2001 Elsevier Science Ltd. All rights reserved.

Keywords: Shape-memory alloy; A. Phase transformation; B. Finite strain; C. Finite elements; C. Numerical alorithms

1. Introduction

At the macroscopic level *shape-memory alloys* (SMA) present the so-called *superelastic effect* (SE). In fact, under loading–unloading cycles — even up to 10–15% strains — the material shows distinct plateaux during the loading and the unloading

* Tel.: + 39-0382-505-476; fax: +39-0382-528-422.
E-mail address: auricchio@unipv.it

PII: S0749-6419(00)00050-4

branches (that is, a stiff-soft-stiff path for both the loading and the unloading), hysteretic response and no permanent deformations.

Due to this distinctive macroscopic behavior, not present in most traditional materials, shape-memory alloys are the basis for innovative applications, ranging from orthodontic wires to self-expanding micro-structures for the treatment of hollow-organ or duct-system occlusions (Duerig et al., 1990; Pelton et al., 1995, 1997).

As always, the macro-behavior finds its justification in the underlying micro-mechanics. In fact, shape-memory alloys present reversible martensitic phase transformations, that is, solid–solid diffusionless transformations between a crystallographically more-ordered phase, the *austenite,* and a crystallographically less-ordered phase, the *martensite* (Wayman 1964; Khachaturyan 1983). At constant temperature, the austenite is typically stable at higher stress values, while the martensite is stable at lower stress values.

If there is no preferred direction for the occurrence of the transformation at the crystallographic level, the martensite takes advantage of the existence of different possible habit planes,[1] forming a series of crystallographically equivalent variants. The product phase is then termed *multiple-variant martensite* and is characterized by a *twinned* structure.

On the other hand, if there is a preferred direction for the occurrence of the transformation (often associated with a state of stress), all the martensitic crystals tend to be generated along the most favorable habit plane. The product phase is then termed *single-variant martensite* and is characterized by a *detwinned* structure.

According to the existence of different single-variant-martensite species, the conversion of a single-variant martensite into a different variant is possible. Such a conversion, known as *reorientation process,* can be also interpreted as another martensitic phase transformation, associated to a non-proportional change of stress.

As highlighted in this brief discussion, the SMA underlying micro-mechanics is quite complex. Moreover, due to the increasing sophistication of SMA-based devices, there is a growing need for effective computational tools able to support the design process.

Accordingly, the goal of the present paper is not in the direction of proposing a new constitutive model for shape-memory materials;[2] in fact, it focuses on the development of a robust and efficient integration algorithm for a model previously discussed in the literature (Auricchio and Taylor, 1997). To reach this goal, Section 2 reviews the time-continuous framework and the specific model, addressing some possible considerations and observations leading to a significative simplification of the model. Section 3 discusses the model time-integration and the algorithmic solution, together with the consistent form of the tangent. Finally, Section 4 tests the proposed approach on a series of severe one-dimensional tests and on a more complex three-dimensional problem.

[1] By definition, the *habit plane* is the contact plane between the austenite and the martensite during a single-crystal transformation (Wayman, 1964; Khachaturyan, 1983).

[2] Without even attempting to be exhaustive, the following References can be taken as examples on the modeling of shape-memory alloy constitutive behavior (Patoor et al., 1988; Achenbach, 1989; Brinson, 1993; Boyd and Lagoudas, 1996; Leclercq and Lexcellent, 1996).

2. A finite-strain superelastic model

We now present a constitutive model able to describe the shape-memory-alloy superelastic response. The model adopted here derives from the one discussed in Auricchio and Taylor (1997) on the basis of previous work (Auricchio, 1995; Auricchio et al., 1997). However, due to new considerations and observations, we are able to recast the model in a format which seems more appropriate for the development of a robust time-discrete solution algorithm.

2.1. Control and internal variables

We assume the deformation gradient, $\mathbf{F}$, as the control variable, and the martensite fraction, ξ_S, as the only scalar internal variable. We also introduce a multiplicative decomposition of $\mathbf{F}$ in the form:

$$\mathbf{F} = \mathbf{F}^e \mathbf{F}^{tr} \tag{1}$$

where $\mathbf{F}^e$ is the elastic part and $\mathbf{F}^{tr}$ is the phase transition part.

So far, the multiplicative split introduced in Eq. (1) is only formal, in the sense that $\mathbf{F}^{tr}$ can be defined as the quota of the deformation gradient depurated by the elastic contribution (that is, $\mathbf{F}^{tr} = (\mathbf{F}^e)^{-1}\ \mathbf{F}$) and it needs to be detailed, as well as related to the internal variable ξ_S, as discussed in Section 2.4.

We wish to stress that a multiplicative split of the deformation gradient in the form presented in Eq. (1) is consistent with a large part of the literature on finite-deformation inelastic models (Lee, 1969; Mandel, 1974). In particular, a review and discussions on the multiplicative split from a computational point of view can be found in Simo and Meschke (1993), Simo (1992, 1998, 1999).

2.2. Elastic constitutive equation

Assuming an isotropic elastic response, the Kirchhoff stress $\boldsymbol{\tau}$ and the elastic left Cauchy–Green tensor $\mathbf{b}^e$, defined as: $\mathbf{b}^e = \mathbf{F}^e \mathbf{F}^{e,T}$, share the same principal directions. Accordingly, the following spectral decompositions can be introduced (Gurtin, 1981):

$$\begin{aligned}
\boldsymbol{\tau} &= \sum_{A=1}^{3} \tau_A \mathbf{n}^A \otimes \mathbf{n}^A \\
\mathbf{t} &= \sum_{A=1}^{3} t_A \mathbf{n}^A \otimes \mathbf{n}^A \\
\mathbf{b}^e &= \sum_{A=1}^{3} \left(\lambda_A^e\right)^2 \mathbf{n}^A \otimes \mathbf{n}^A
\end{aligned} \tag{2}$$

with λ_A^e the elastic stretches[3] and $\mathbf{t}$ the deviatoric part of $\boldsymbol{\tau}$, according to the relation:

$$\boldsymbol{\tau} = p\mathbf{1} + \mathbf{t} \tag{3}$$

where $\mathbf{1}$ is the second-order identity tensor, p is the pressure, defined as $p = \mathrm{tr}(\boldsymbol{\tau})/3$, and tr() is the trace operator.

Due to the isotropy assumption, the material free-energy ψ is an isotropic function of $\mathbf{b}^e$, hence, it can be expressed in terms of $\left(\lambda_A^e\right)^2$:

$$\psi = \psi\left[\left(\lambda_A^e\right)^2\right] \tag{4}$$

The Kirchhoff stress components would then be given by:

$$\tau_A = 2\frac{\partial\psi}{\partial\left[\left(\lambda_A^e\right)^2\right]}\left(\lambda_A^e\right)^2 \tag{5}$$

Introducing the elastic volume J^e and the deviatoric elastic stretches $\bar{\lambda}_A^e$:

$$J^e = \lambda_1^e\lambda_2^e\lambda_3^e, \quad \bar{\lambda}_A^e = (J^e)^{-\frac{1}{3}}\lambda_A^e \tag{6}$$

as well as the corresponding logarithmic quantities:

$$\theta^e = \log(J^e), \quad e_A^e = \log(\bar{\lambda}_A^e) \tag{7}$$

we assume a free-energy uncoupled in a deviatoric and a volumetric contribution, as follows:

$$\psi = U(\theta^e) + W(e_A^e) = \frac{1}{2}K[\theta^e] + G\sum_{A=1}^{3}\left[e_A^e\right]^2 \tag{8}$$

with K and G the bulk and the shear elastic moduli, respectively. Hence, exploiting Eq. (5) and recalling Eq. (3), we deduce that:

$$\tau_A = p + t_A \tag{9}$$

with:

$$p = K\theta^e, \quad t_A = 2Ge_A^e \tag{10}$$

[3] The quantities λ_A^e should be called more properly as "elastic principal stretches". However, since in all the forthcoming discussions, we work in principal directions, for brevity we omit the word "principal".

2.3. Phase transformations and activation conditions

We consider two phase transformations: the conversion of austenite into martensite ($A \rightarrow S$) and the conversion of martensite into austenite ($S \rightarrow A$). To model the possible phase-transformation pressure-dependence (Kakeshita et al., 1992), we introduce a Drucker–Prager-type loading function:

$$F(\boldsymbol{\tau}) = \|\mathbf{t}\| + 3\alpha p \tag{11}$$

where α is a material parameter and $||\cdot||$ indicates the Euclidean norm, such that:

$$\|\mathbf{t}\| = \left[\sum_{A=1}^{3} (t_A)^2\right]^{1/2} \tag{12}$$

Indicating variations in time with a superposed dot, we assume the following linear forms for the evolution of ξ_S:

$$\dot{\xi}_S = H^{AS}(1 - \xi_S)\frac{\dot{F}}{F - R_F^{AS}} \tag{13}$$

$$\dot{\xi}_S = H^{SA}\xi_S\frac{\dot{F}}{F - R_f^{SA}} \tag{14}$$

where:

$$R_f^{AS} = \left[\sigma_f^{AS}\left(\sqrt{\frac{2}{3}} + \alpha\right)\right], \quad R_f^{SA} = \left[\sigma_f^{SA}\left(\sqrt{\frac{2}{3}} + \alpha\right)\right] \tag{15}$$

with $\sigma_s^{AS}, \sigma_f^{AS}, \sigma_s^{SA}, \sigma_f^{SA}$ material constants. The scalar quantities H^{AS} and H^{SA} embed the phase-transformation activation conditions — hence, allowing to choose between Eqs. (13) and (14) — and they are defined by the relations:

$$H^{AS} = \begin{cases} 1 & \text{if } \begin{cases} R_s^{AS} < F < R_f^{AS} \\ \dot{F} > 0 \end{cases} \\ 0 & \text{otherwise} \end{cases} \tag{16}$$

$$H^{SA} = \begin{cases} 1 & \text{if } \begin{cases} R_f^{SA} < F < R_s^{SA} \\ \dot{F} < 0 \end{cases} \\ 0 & \text{otherwise} \end{cases} \tag{17}$$

where:

$$R_s^{AS} = \left[\sigma_s^{AS}\left(\sqrt{\frac{2}{3}}+\alpha\right)\right], \quad R_s^{SA} = \left[\sigma_s^{SA}\left(\sqrt{\frac{2}{3}}+\alpha\right)\right] \tag{18}$$

2.4. Strain decomposition

The only ingredient we still need to specify is the relation between the internal variable ξ_S and the transformation part of the deformation gradient $\mathbf{F}^{tr}$. To do so, introduced the transformation left Cauchy–Green tensor $\mathbf{b}^{tr}$, defined as:

$$\mathbf{b}^{tr} = \mathbf{F}^{tr}\mathbf{F}^{tr,T} \tag{19}$$

we assume for $\mathbf{b}^{tr}$ the same spectral decomposition as for $\boldsymbol{\tau}$ and $\mathbf{b}^{\mathrm{e}}$:

$$\mathbf{b}^{tr} = \sum_{A=1}^{3}\left(\lambda_A^{tr}\right)^2 \mathbf{n}^A \otimes \mathbf{n}^A \tag{20}$$

Accordingly, we have that:

$$\mathbf{b} = \mathbf{F}\mathbf{F}^T = \mathbf{b}^e\mathbf{b}^{tr} = \mathbf{b}^{tr}\mathbf{b}^e \tag{21}$$

and:

$$\mathbf{b} = \sum_{A=1}^{3}(\lambda_A)^2 \mathbf{n}^A \otimes \mathbf{n}^A \tag{22}$$

Introducing the logarithmic strains:

$$\epsilon_A = \log(\lambda_A), \quad \epsilon_A^e = \log\left(\lambda_A^e\right), \quad \epsilon_A^{tr} = \log\left(\lambda_A^{tr}\right) \tag{23}$$

we get an additive logarithmic strain decomposition:

$$\epsilon_A = \epsilon_A^e + \epsilon_A^{tr} \tag{24}$$

which can be rewritten in terms of the volumetric and deviatoric quantities as follows:

$$\theta = \theta^e + \theta^{tr} \ , \quad e_A = e_A^e + e_A^{tr} \tag{25}$$

with:

$$\begin{array}{rclcrcl} \theta & = & \log(J) & , & e_A & = & \log\left(\bar{\lambda}_A\right) \\ \theta^{tr} & = & \log(J^{tr}) & , & e_A^{tr} & = & \log\left(\bar{\lambda}_A^{tr}\right) \\ J & = & \lambda_1\lambda_2\lambda_3 & , & \bar{\lambda}_A & = & (J)^{-\frac{1}{3}}\lambda_A \\ J^{tr} & = & \lambda_1^{tr}\lambda_2^{tr}\lambda_3^{tr} & , & \bar{\lambda}_A^{tr} & = & (J^{tr})^{-\frac{1}{3}}\lambda_A^{tr} \end{array} \tag{26}$$

Finally, we set:

$$\epsilon_A^{tr} = \epsilon_L \xi_S N_A \tag{27}$$

where ε_L is a scalar parameter representing the maximum deformation, obtainable only by detwinning of the multiple-variant martensite. Moreover, introducing the notation:

$$x_A = \mathbf{x}|_A \tag{28}$$

to extract the A-component from a generic $\mathbf{x}$ vector, we have:

$$N_A = \mathbf{N}|_A = \left[\frac{\partial F}{\partial \boldsymbol{\tau}}\right]\Bigg|_A = \mathbf{n} + \alpha \mathbf{1}|_A = n_A + \alpha \tag{29}$$

with:

$$n_A = \frac{t_A}{\|\mathbf{t}\|} \tag{30}$$

It is interesting to observe that, combining Eqs. (20), (23) and (27), the proposed formulation seems to recall the formalism of deformation plasticity and not of the more classical flow theory of plasticity. However, we wish to stress that, first of all, the consistency between a flow plasticity theory and the proposed approach has been discussed in Auricchio (1995) and in Auricchio et al. (1997). Moreover, the major justification of the proposed approach can be found in the different physics behind typical plastic flow phenomena and martensitic transformations (in particular, in the light of reorientation processes for the martensitic variants).

Finally, combining Eqs. (10), (25) and (27), we get:

$$p = K(\theta - 3\alpha\epsilon_L \xi_S) \tag{31}$$

$$t_A = 2G(e_A - \epsilon_L \xi_S n_A) \tag{32}$$

2.5. Remarks and consequent modifications

We now show that it is possible to reformulate Eq. (32) in an equivalent but simpler form, more suitable for a robust algorithmic solution, as discussed in Section 3.

Combining Eqs. (30) and (32), we get:

$$(\|\mathbf{t}\| + 2G\epsilon_L \xi_S) n_A = 2G e_A \tag{33}$$

and noting that:

$$\|\mathbf{t}\| \geqslant 0$$
$$\epsilon_L \xi_S \geqslant 0$$
$$2G > 0 \tag{34}$$

we conclude that:

$$(\|\mathbf{t}\| + 2G\epsilon_L \xi_S) = 2G\|\mathbf{e}\| \tag{35}$$

hence:

$$n_A = d_A \stackrel{\text{def}}{=} \frac{e_A}{\|\mathbf{e}\|} \tag{36}$$

Accordingly, Eq. (32) can be rewritten as:

$$t_A = 2G(e_A - \epsilon_L \xi_S d_A) \tag{37}$$

It is worth emphasizing the difference between Eqs. (32) and (37). In fact, in the realm of a strain-driven process (which is the case of classical integration algorithm), the right hand side of Eq. (32) contains two unknowns, i.e. n_A and ξ_S; on the other hand, the right hand side of Eq. (37) contains only one unknown, i.e. ξ_S since the quantity d_A can be easily computed in terms of the strain components.

3. Time-discrete model and solution algorithm

We now discuss the integration in time of the model addressed in the previous section, together with a robust solution algorithm.[4] We conclude the section presenting the form of the tangent consistent with the time-discrete algorithm.

3.1. Time-discrete model

The time-discrete model is obtained integrating the time-continuous model over the time interval $[t_n,t]$;[5] in particular, we use a backward-Euler integration formula for the rate-equations, evaluating all the non-rate equations at time t. Accordingly, we get:

$$p = K(\theta - 3\alpha\epsilon_L \xi_S) \tag{38}$$

[4] To simplify the notation and recalling that all the quantities of interest share the principal directions, from now on we we use as extensively as possible the vector notation referred to the principal directions. Accordingly, a bold-face letter will indicate a three-component vector; as an example, given the generic vector $\mathbf{x}$, x_A indicates its A-th component with $A = 1,2,3$, i.e.: $x_A = \mathbf{x}|_A$.

[5] To minimize the appearance of subscripts, the subscript n indicates a quantity that is evaluated at time t_n, while no subscript indicates a quantity that is evaluated at time t, with $t_n < t$.

$$\mathbf{t} = 2G(\mathbf{e} - \epsilon_L \xi_S \mathbf{d}) \tag{39}$$

with:

$$\mathbf{d} = \frac{\mathbf{e}}{\|\mathbf{e}\|} \tag{40}$$

Written in residual form and clearing fractions, the time-discrete evolutionary equations specialize to:

$$\mathcal{R}^{AS} = \left(F - R_f^{AS}\right)\lambda_S + H^{AS}(1 - \xi_S)(F - F_n) = 0 \tag{41}$$

$$\mathcal{R}^{SA} = \left(F - R_f^{SA}\right)\lambda_S - H^{SA}\xi_S(F - F_n) = 0 \tag{42}$$

where:

$$\lambda_S = \int_{t_n}^{t} \dot{\xi}_S dt = \xi_S - \xi_{S,n} \tag{43}$$

The quantity λ_S can be computed expressing F as a function of λ_S and requiring the satisfaction of the discrete equation relative to the corresponding active phase transition.

It is also interesting to note that, due to the simple case presented here and limited only to two phase transitions, Eqs. (13) and (14) can be easily integrated in closed form (Auricchio and Lubliner, 1997). However, we prefer to solve the fraction evolution through a classical integration scheme in time, since this approach could be generalized to more complex situations, such as the case of multiple phase transitions.

3.2. Solution algorithm

Considering the time-discrete problem as deformation driven, we assume to know **F,** i.e. the deformation gradient at time t, as well as $\mathbf{F}_n$ and $\xi_{S,n,}$, i.e. the deformation gradient and the martensite fraction at time t_n.

The proposed solution algorithm can be cast within the return-map family. Initially suggested for plasticity (Maenchen and Sack, 1964; Wilkins, 1964), return-map schemes often provide efficient and robust solution algorithm based on a discrete enforcement of the evolutionary equations (Simo and Hughes, 1998; Simo, 1999).

Following the return-map philosophy, the adopted algorithm consists of two parts. Initially, an elastic *predictor* or *trial state* is computed; then, if the trial state violates the constitutive model, an *inelastic correction* is computed using the trial state as an initial condition. The details of the algorithm are presented in Table 1 while in the following we comment on some non-trivial aspects.

To compute the trial state, we assume that in the time interval $[t_n,t]$ there is no martensite fraction evolution. Accordingly, indicating the trial values with a superscript TR, we set:

Table 1
Solution algorithm for the time-discrete model

1. Spectral decomposition
Compute spectral decomposition of b
Compute $\mathbf{n}^{\mathrm{A}}$, d_{A} and λ_{A}
Compute ϵ_{A}, θ and e_{A}

2. Compute β
Compute $||\mathbf{e}||$
Depending on $\|e\| - \epsilon_L \xi_{S,n}$ set β

3. Compute trial state
Assume no phase transformations ($\lambda_{\mathrm{S}} = 0$)
Compute p^{TR}, $\mathbf{t}^{\mathrm{TR}}$, $\mathrm{F}^{\mathrm{AS,TR}}$

4. Check phase transformations
if (PT conditions satisfied) then
    compute martensite increment
    update martensite fraction
    update stress
end if

5. Compute algorithmic tangent

$$\begin{aligned} \lambda_S^{TR} &= 0 \\ p^{TR} &= K(\theta - 3\alpha\epsilon_L\xi_{S,n}) \\ \mathbf{t}^{TR} &= 2G(\mathbf{e} - \epsilon_L\xi_{S,n}\mathbf{d}) \end{aligned} \tag{44}$$

We may observe that Eq. $(44)_3$ can be rewritten as:

$$\left\|\mathbf{t}^{TR}\right\|\mathbf{n}^{TR} = 2G\big(\|\mathbf{e}\| - \epsilon_L\xi_{S,n}\big)\mathbf{n} \tag{45}$$

where we use the relation $\mathbf{d} = \mathbf{n}$; however, relation 45 does not necessarily imply that:

$$\mathbf{n}^{TR} = \mathbf{n} \tag{46}$$

The fact that $\mathbf{n}^{TR}$ and $\mathbf{n}$ do not necessarily coincide makes the present algorithm somehow different from the ones often adopted in plasticity (Auricchio and Taylor, 1999). However, a relation between $\mathbf{n}^{TR}$ and $\mathbf{n}$ can be obtained also in this case and, as a consequence, we are able to construct a radial return algorithm also for the present model. In fact, from Eq. (45) we get that:

$$\mathbf{n}^{TR} = \beta\mathbf{d} \tag{47}$$

with:

$$\begin{aligned} \beta &= \quad 1 \quad \text{if} \quad \left(\|\mathbf{e}\| - \epsilon_L \xi_{S,n}\right) > 0 \\ \beta &= -1 \quad \text{if} \quad \left(\|\mathbf{e}\| - \epsilon_L \xi_{S,n}\right) < 0 \end{aligned} \tag{48}$$

As a consequence we obtain a scalar relation between the norm of the deviatoric stress and the norm of the trial deviatoric stress, as discussed in the following. Combining Eqs (39), (43) and (44), we get:

$$\mathbf{t} = \mathbf{t}^{TR} - 2G\epsilon_L \lambda_S \mathbf{d} \tag{49}$$

and recalling that $\mathbf{n} = \mathbf{d}$, we obtain:

$$\|\mathbf{t}\|\mathbf{d} = \left\|\mathbf{t}^{TR}\right\|\beta\mathbf{d} - 2G\epsilon_L \lambda_S \mathbf{d} \tag{50}$$

Hence:

$$\|t\| = \left\|t^{TR}\right\|\beta - 2G\epsilon_L \lambda_S \tag{51}$$

We may now express the loading function in terms of the trial values as follows:

$$F = F^{AS,TR} - \lambda_S \Delta \tag{52}$$

with:

$$\begin{aligned} F^{AS,TR} &= \left\|\mathbf{t}^{TR}\right\|\beta + 3\alpha p^{TR} \\ \Delta &= \left(2G + 9\alpha^2 K\right)\epsilon_L \end{aligned} \tag{53}$$

Substituting in the time-discrete evolutionary equations, we can finally solve with respect to λ_S:

$$\lambda_S = A\left(F^{AS,TR} - F_n\right) \tag{54}$$

with:

$$A = \frac{(1 - \xi_{S,n})}{\left[\left(R_f^{AS} - F_n\right) + (1 - \xi_{S,n})\Delta\right]} \quad \text{for} \quad H^{AS} = 1 \tag{55}$$

$$A = \frac{-\xi_{S,n}}{\left[\left(R_f^{SA} - F_n\right) - \xi_{S,n}\Delta\right]} \quad \text{for} \quad H^{SA} = 1 \tag{56}$$

3.3. Algorithmic tangent

We now address the consistent linearization of the time-discrete model. In fact, the use of a consistent tangent preserves the quadratic convergence of the Newton

method, which we adopt for the incremental solution of the finite-element scheme in Sections 4 and 4.2.

Linearizing the elastic constitutive relations (38) and (39), we get:

$$dp = K(d\theta - 3\alpha\epsilon_L d\lambda_S) \tag{57}$$

$$d\mathbf{t} = 2G[de - \epsilon_L(d\lambda_S \mathbf{d} + \xi_S d\mathbf{d})] \tag{58}$$

It is possible to show that:

$$d\mathbf{d} = d\left(\frac{\mathbf{e}}{\|\mathbf{e}\|}\right) = \frac{1}{\|\mathbf{e}\|}[\mathbf{I} - \mathbf{d} \otimes \mathbf{d}]d\mathbf{e} \tag{59}$$

where $\mathbf{I}$ is the identity matrix. Accordingly:

$$dp = Kd\theta - 3K\alpha\epsilon_L d\lambda_S \tag{60}$$

$$d\mathbf{t} = 2G\left[I - \epsilon_L \xi_S \frac{1}{\|\mathbf{e}\|}(\mathbf{I} - \mathbf{d} \otimes \mathbf{d})\right]d\mathbf{e} - 2G\epsilon_L \mathbf{d} d\lambda_S \tag{61}$$

The scalar quantity $d\lambda_S$ is computed from the linearization of the active discrete-time evolutionary equation $\mathcal{R}$, considered as a function of ϵ and λ_S. Accordingly:

$$\mathcal{R}(\lambda_S, \boldsymbol{\epsilon}) = 0 \;\Rightarrow\; d\mathcal{R} = \frac{\partial \mathcal{R}}{\partial \lambda_S} d\lambda_S + \frac{\partial \mathcal{R}}{\partial \boldsymbol{\epsilon}} d\boldsymbol{\epsilon} = 0 \tag{62}$$

which can be solved for $d\lambda_S$:

$$d\lambda_S = \left[\frac{\partial \mathcal{R}}{\partial \lambda_S}\right]^{-1} \frac{\partial \mathcal{R}}{\partial \boldsymbol{\epsilon}} \tag{63}$$

For the particular evolutionary equations under investigation, we obtain:

$$d\lambda_S = A(2G\mathbf{n} + 3K\mathbf{1}) : d\boldsymbol{\epsilon} \tag{64}$$

with A defined in Eqs. (55)–(56). Finally, we obtain:

$$d\boldsymbol{\tau} = \mathbf{D} d\boldsymbol{\epsilon} \tag{65}$$

where:

$$\mathbf{D} = \left[K^\star(\mathbf{1} \otimes \mathbf{1}) + 2G^\star \mathbf{I}_{dev} + M_1^\star(\mathbf{d} \otimes \mathbf{d}) - M_2^\star(\mathbf{d} \otimes \mathbf{1} + \mathbf{1} \otimes \mathbf{d})\right] \tag{66}$$

with:

$$
\begin{aligned}
K^{\star} &= K\left\{1 - 9K\epsilon_L\alpha^2 A\right\} \\
G^{\star} &= G\left\{1 - \frac{\epsilon_L \xi_S}{\|\mathbf{e}\|}\right\} \\
M_1^{\star} &= 2G\epsilon_L\left[\frac{\xi_S}{\|\mathbf{e}\|} - 2GA\right] \\
M_2^{\star} &= 2G\epsilon_L 3K\alpha A
\end{aligned}
\tag{67}
$$

4. Numerical examples

To verify to robustness of the proposed algorithm, we start with a careful and extensive investigation on a set of one-dimensional tests and, then, we study a more complex three-dimensional problem.

4.1. One-dimensional tests

We consider a cubic specimen with side equal to 1 mm, loaded controlling the displacement in a direction parallel to one specimen side. The boundary conditions are set to reproduce a uniaxial state of stress during the loading.

We then consider four materials (Table 2) and four loading histories[6] (Table 3) and, to properly test the algorithm, we run all the possible combinations between material properties and loading histories. For all the Materials we set:

$$
v = 0.3\,,\ \epsilon_L = 0.07 \tag{68}
$$

noting that, given $\sigma_s^{AS,+}$ and $\sigma_s^{AS,-}$ the parameter α can be computed as follows:

$$
\alpha = \sqrt{\frac{2}{3}}\frac{\sigma_s^{AS,-} - \sigma_s^{AS,+}}{\sigma_s^{AS,-} + \sigma_s^{AS,+}} \tag{69}
$$

Moreover, we observe that:

- Loads 1 and 2 are the same but they are solved with two different time increments, a smaller one ($\mathrm{d}t = 0.02$ s) and a larger one ($\mathrm{d}t = 0.2$ s), respectively.
- Loads 3 and 4 differ from Load 1 and Load 2 only in the peak values. Both Loads 3 and 4 are solved with the larger time increment ($\mathrm{d}t = 0.2$ s).
- Material 2 is characterized by flat plateaux for both the forward and the reverse phase transformations.
- Material 3 is characterized by flat plateaux for both the forward and the reverse phase transformations and a very high elastic modulus.

[6] The loading histories are described in terms of a time scale, which however should be considered simply as a pseudo-time variable, being the model time-independent.

Table 2
One-dimensional tests: material properties. Four different materials are considered

Material number	E [MPa]	$\sigma_s^{AS,+}$	$\sigma_f^{AS,+}$	$\sigma_s^{SA,+}$	$\sigma_f^{SA,+}$	$\sigma_s^{AS,-}$
1	5×10^4	520	600	300	200	700
2	5×10^4	500	500	300	300	700
3	5×10^6	500	500	300	300	700
4	5×10^4	500	500	1	1	700

Table 3
One-dimensional tests: loading histories. Four different loading histories are considered

Load 1		Load 2		Load 3		Load 4	
Time (s)	Displ (mm)	Time (s)	Displ (mm)	Time (s)	Displ (mm)	Time (s)	Displ (mm)
0	0.0	0	0.0	0	0.0	0	0.0
1	1.0	1	1.0	1	0.9	1	1.1
3	−1.0	3	−1.0	3	−1.1	3	−0.9
5	−1.0	5	−1.0	5	0.9	5	−1.1

- Material 4 is characterized by flat plateaux for both the forward and the reverse phase transformations and a very small (practically zero) stress value for the reverse phase transformation.

For each simulation we report the response in terms of Kirchhoff stress versus displacement (Figs. 1–4), presenting in general the plots only for the area of major interest (i.e. the ones where it is possible to observe the phase transformations). The solutions relative to Load 1 (i.e. the case integrated with $dt = 0.02$ s) are reported with a continuous line and no symbols, while the solutions relative to the other loading cases (i.e. the cases integrated with $dt = 0.2$ s) are reported with lines and symbols (dot lines and circles for Load 2, dash-dot lines and crosses for Load 3, dash lines and diamonds for Load 4). In particular, we wish to note that for the last three loading cases there is a correspondence between symbols and instants at which the discrete solutions are computed.

For all the cases studied, it is possible to observe the optimal placements of the time-discrete solutions despite the quite large time-integration step adopted for the numerical solutions.

4.2. An orthodontic archwire

To test the proposed algorithm in a more complex situation, we now consider the simulation of the orthodontic archwire, sketched in Fig. 5. The dimensions are taken from Raboud (1998) and they are reported in Table 4 for all the segment indicated in Fig. 5. Moreover, we assume that the archwire is made out of a wire with rectangular

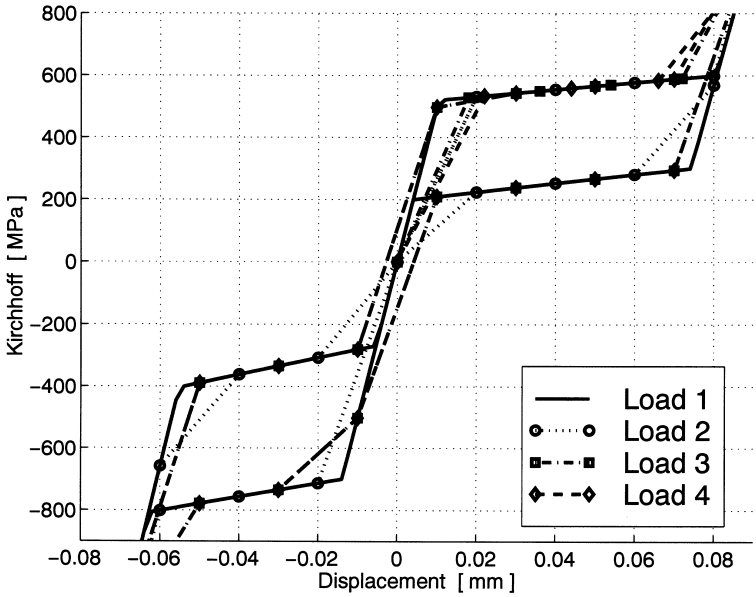

Fig. 1. One-dimensional test: Material 1. Kirchhoff stress versus displacement.

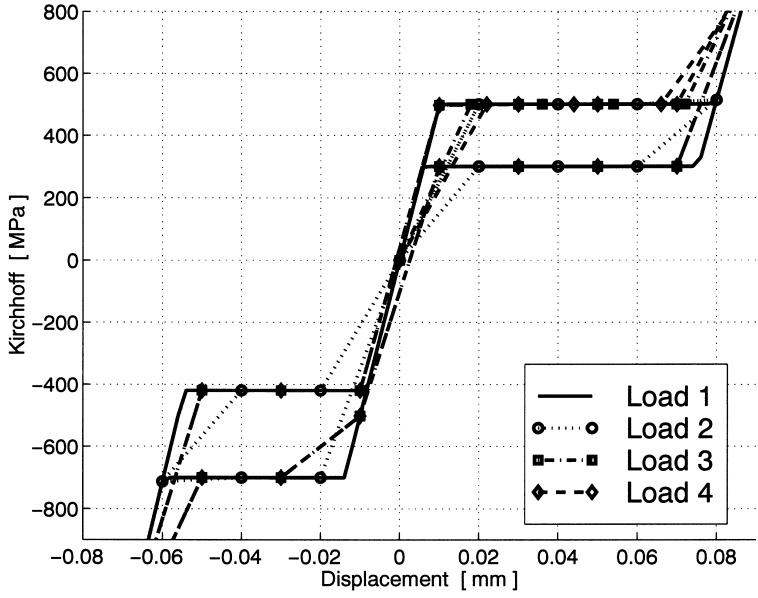

Fig. 2. One-dimensional test: Material 2. Kirchhoff stress versus displacement.

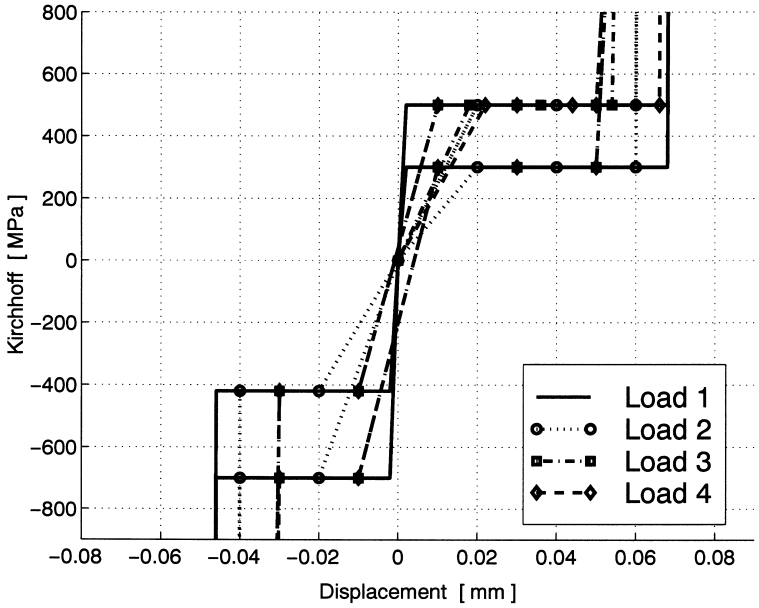

Fig. 3. One-dimensional test: Material 3. Kirchhoff stress versus displacement.

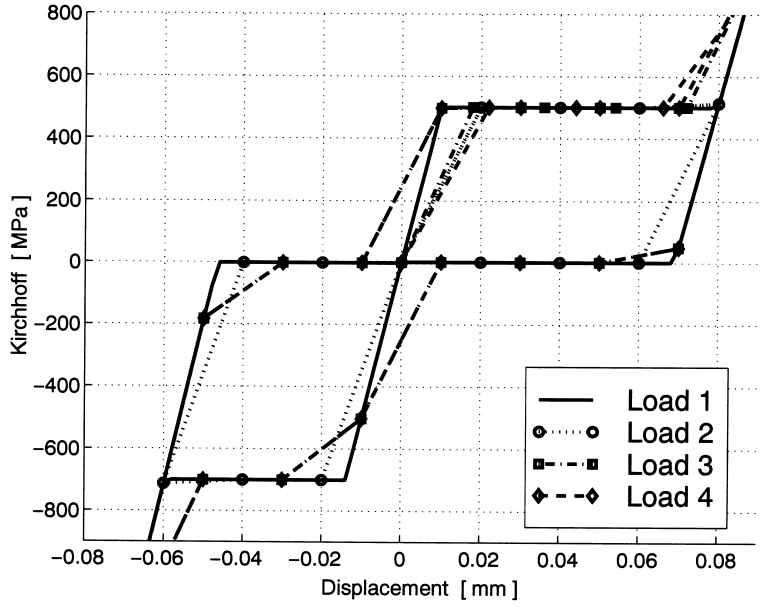

Fig. 4. One-dimensional test: Material 4. Kirchhoff stress versus displacement.

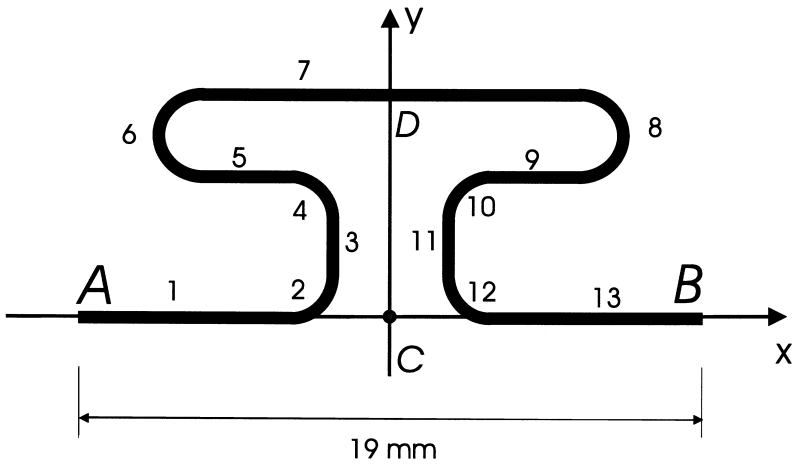

Fig. 5. Orthodontic archwire: geometry data.

Table 4
Orthodontic archwire: details on the geometry. The segment numbers are indicated in Fig. 5

Segment number	Segment type	Length (mm)	Angle (°)	Radius (mm)
1	Straight	7.5	–	–
2	Circular	–	90	1
3	Straight	2.0	–	–
4	Circular	–	90	1
5	Straight	2.5	–	–
6	Circular	–	180	1
7	Straight	9.0	–	–
8	Circular	–	180	1
9	Straight	2.5	–	–
10	Circular	-	90	1
11	Straight	2.0	–	–
12	Circular	–	90	1
13	Straight	7.5	–	–

0.635×0.432 mm cross-section. The archwire material properties are set equal to ones relative to Material 2 in the previous set of analyses.

The archwire is loaded imposing outward displacements, equal in magnitude, on sections A and B (Fig. 5). In particular, starting from the undeformed configuration, we reach a maximum displacement of 7 mm in 7 s, then bringing back to zero the imposed displacement in other 7 s.

Due to geometric and loading symmetry considerations, in the analysis we consider only half of the archwire, introducing proper boundary conditions on the C-D plane to reproduce the symmetry conditions (Fig. 5). In particular, Fig. 6 shows the

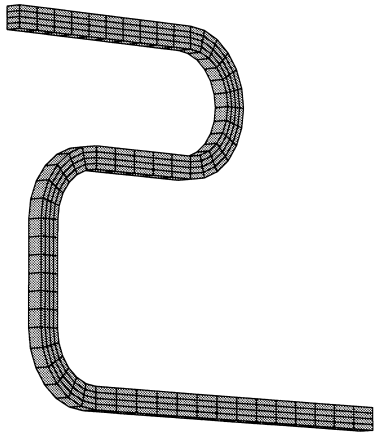

Fig. 6. Orthodontic archwire: undeformed mesh.

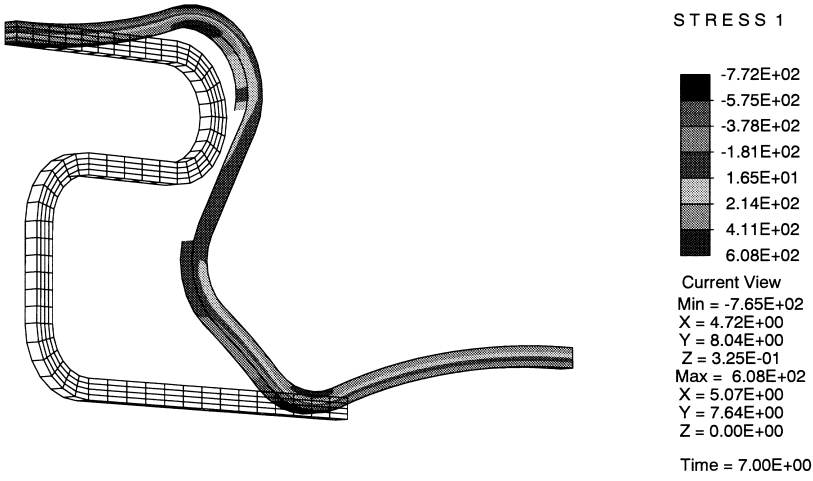

Fig. 7. Orthodontic archwire: deformed mesh in the maximum deformed configuration.

mesh in the undeformed configuration, while Fig. 7 shows the maximum deformed configuration ($t = 7$ s) in combination with a contour plot for the first component of stress tensor.

5. Closure and future research directions

The present work proposes a further step toward the development of a computation tool to be used during the design of SMA-based devices.

To reach this goal, we review a constitutive model able to reproduce the superelastic behavior at finite strains. The model derives from the one discussed in Reference (Auricchio and Taylor, 1997); however, due to new considerations and observations, we present the model in a format which is more appropriate for the development of a robust time-discrete solution algorithm.

We then discuss a solution algorithm for the corresponding time-discrete model. Cast within the return-map family, the adopted approach pays particular attention to the overall algorithmic robustness and to the possibility of an efficient implementation. In particular, we show how it is possible to perform a radial return also for the model under investigation.

To properly test the proposed numerical scheme, we study a careful and extensive investigation on a set of one-dimensional tests and a more complex three-dimensional problem, relative to an orthodontic archwire. All the numerical simulations presented show that the proposed approach is robust and viable.

Future research will try to extend the proposed integration algorithm to more complex constitutive models relative to shape memory materials. In particular, we will investigate the combined modeling of the superelastic effect and of the shape-memory effect.

Acknowledgements

The author would like to acknowledge Dr. John Hallquist and Dr. Nielen Stander of Livermore Software Technology Company (LSTC), Livermore (CA) for initial discussions on the subject of the present paper as well as the Italian National Center of Research (C.N.R) for partial support through the "Second Special Project for Advanced Technologies" ("Materiali Speciali per Tecnologie Avanzate II").

References

Achenbach, M., 1989. A model for an alloy with shape memory. International Journal of Plasticity 5, 371–395.

Auricchio, F., 1995. Shape-Memory Alloys: Applications, Micromechanics, Macromodelling and Numerical Simulations. PhD dissertation, University of California at Berkeley, Department of Civil Engineering.

Auricchio, F., Lubliner, J., 1997. A uniaxial model for shape-memory alloys. International Journal of Solids and Structures 34, 3601–3618.

Auricchio, F., Taylor, R., 1997. Shape-memory alloys: modelling and numerical simulations of the finite-strain superelastic behavior. Computer Methods in Applied Mechanics and Engineering 143, 175–194.

Auricchio, F., Taylor, R., 1999. A return-map algorithm for general associative isotropic elasto-plastic materials in large deformation regimes. International Journal of Plasticity 15, 1359–1378.

Auricchio, F., Taylor, R., Lubliner, J., 1997. Shape-memory alloys: macromodelling and numerical simulations of the superelastic behavior. Computer Methods in Applied Mechanics and Engineering 146, 281–312.

Boyd, J., Lagoudas, D., 1996. A thermodynamical constitutive model for shape-memory materials. Part I. The monolithic shape-memory alloy. International Journal of Plasticity 12, 805–842.

Brinson, L., 1993. One-dimensional constitutive behavior of shape memory alloys: Thermomechanical derivation with non-constant material functions and redefined martensite internal variables. Journal of Intelligent Material Systems and Structures 4, 229–242.

Duerig, T., Melton, K., Stökel, D., Wayman, C., (Eds.), 1990. Engineering Aspects of Shape Memory Alloys. Butterworth-Heinemann.

Gurtin, M., 1981. An Introduction to Continuum Mechanics. Academic Press.

Kakeshita, T., Shimizu, K., Nakamichi, S., Tanaka, R., Endo, S., Ono, F., 1992. Effect of hydrostatic pressures on thermoelastic martensitic transformations in aged Ti–Ni and ausaged Fe–Ni–Co–Ti shape memory alloys. Materials Transactions JIM 33, 1–6.

Khachaturyan, A., 1983. Theory of Structural Transformations in Solids. John Wiley & Sons.

Leclercq, S., Lexcellent, C., 1996. A general macroscopic description of the thermomechanical behavior of shape memory alloys. Journal of Mechanics and Physics of Solids 44, 953–980.

Lee, E., 1969. Elastic-plastic deformation at finite strains. Journal of Applied Mechanics 36, 1–6.

Maenchen, G., Sack, S., 1964. The tensor code. In: Alder, B. (Ed.), Methods in Computational Physics, Volume 3. Academic Press, pp. 181–210.

Mandel, J., 1974. Thermodynamics and plasticity. In: Dominger, J.D., Nina, M., Whitelaw, J. (Eds.), Foundations of Continuum Thermodynamics, pp. 283–304.

Patoor, E., Eberhardt, A., Berveiller, M., 1988. Thermomechanical behaviour of shape memory alloys. Archives of Mechanics 40, 755–794.

Pelton, A., Hodgson, D., Duerig, T. (Eds.), 1995. Proceedings of the First International Conference on Shape Memory and Superelastic Technologies, Asilomar, CA.

Pelton, A., Hodgson, D., Russel, S., Duerig, T. (Eds.), 1997. Proceedings of the Second International Conference on Shape Memory and Superelastic Technologies, Asilomar, CA.

Raboud, D., 1998. Simulation of the superelastic response of SMA orthodontic wires. Journal of Biomechanical Engineering 120, 676–685.

Simo, J., 1992. Algorithms for static and dynamic multiplicative plasticity that preserve the classical return mapping schemes of the infinitesimal theory. Computer Methods in Applied Mechanics and Engineering 99, 61–112.

Simo, J., 1999. Topics on the numerical analysis and simulation of plasticity. In: Ciarlet, P. Lions, J. (Eds.), Handbook of Numerical Analysis, Volume III. Elsevier Science Publisher BV, Amsterdam.

Simo, J., Hughes, T., 1998. Computational Inelasticity. Springer-Verlag.

Simo, J., Meschke, G., 1993. A new class of algorithms for classical plasticity extended to finite strains, applications to geomaterials. Computational Mechanics 11, 253–278.

Wayman, C., 1964. Introduction to the Crystallography of Martensitic Transformations. MacMillan.

Wilkins, M., 1964. Calculation of elastic plastic flow. In: Alder, B. (Ed.), Methods in Computational Physics, Volume 3. Academic Press, pp. 211–263.